Evaluation of correlated Pandora column NO$_2$ and *in situ* surface NO$_2$ measurements during GMAP campaign

Lim-Seok Chang[1], Donghee Kim[1], Hyunkee Hong[1], Deok-Rae Kim[1], Jeonga Yu[1],

Kwangyul Lee[1], Hanlim Lee[2], Daewon Kim[2], Jinkyu Hong[3], Hyun-Young Jo[4],

and Cheol-Hee Kim[4, 5]

[1] *Environmental Satellite Center, National Institute of Environmental Research, Incheon, 22689, Republic of Korea*

[2] *Department of Spatial Information Engineering, Pukyong National University, Busan, 48547, Republic of Korea*

[3] *Department of Atmospheric Sciences, Yonsei University, Seoul, 03722, Republic of Korea*

[4] *Institute of Environmental Studies, Pusan National University, Busan, 46241, Republic of Korea*

[5] *Department of Atmospheric Sciences, Pusan National University, Busan, 46241, Republic of Korea*

Correspondence:

Cheol-Hee Kim (chkim2@pusan.ac.kr), and Lim-Seok Chang (lschang@korea.kr)

Abstract.

To validate the Geostationary Environment Monitoring Spectrometer (GEMS), the GEMS Map of Air Pollution (GMAP) campaign was conducted during 2020–2021 by integrating Pandora Asia Network, aircraft, and *in situ* measurements. In the present study, GMAP-2020 measurements were applied to evaluate urban air quality and explore the synergy of Pandora column (PC) NO_2 measurements and surface *in situ* (SI) NO_2 measurements for Seosan, South Korea, where large point source (LPS) emissions are densely clustered. Due to the difficulty of interpreting the effects of LPS emissions on air quality downwind of Seosan using SI monitoring networks alone, we explored the combined analysis of both PC-NO_2 and SI-NO_2 measurements. Agglomerative hierarchical clustering using vertical meteorological variables combined with PC-NO_2 and SI-NO_2 yielded three distinct conditions: synoptic wind-dominant (SD), mixed (MD), and local wind-dominant (LD). These results suggest meteorology-dependent correlations between PC-NO_2 and SI-NO_2. Overall, yearly daytime mean (11:00–17:00 KST) PC-NO_2 and SI-NO_2 statistical data showed good linear correlations ($R = {\sim}0.73$); however, the differences in correlations were largely attributed to meteorological conditions. SD conditions characterized by higher wind speeds and advected marine boundary layer heights suppressed fluctuations in both PC-NO_2 and SI-NO_2, driving a uniform vertical NO_2 structure with higher correlations, whereas under LD conditions, LPS plumes were decoupled from the surface or were transported from nearby cities, weakening correlations through anomalous vertical NO_2 gradients. The discrepancies suggest that using either PC-NO_2 or SI-NO_2 observations alone involves a higher possibility of uncertainty under LD conditions or prevailing transport processes. However, under MD conditions, both pollution ventilation due to high surface wind speeds and daytime photochemical NO_2 loss contributed to stronger correlations through a decline in both PC-NO_2 and SI-NO_2 toward noon. Thus, Pandora Asia Network observations collected over 13 Asian countries since 2021 can be utilized for detailed investigation of the vertical complexity of air quality, and the conclusions can be also applied when performing GEMS observation interpretation in combination with SI measurements.

1. Introduction

Rapid developments in environmental remote sensing have led to a new era of air quality observations, and recent hyperspectral data retrieval technologies have allowed for routine and

32 accurate monitoring of air pollutants at high spatial and temporal resolution. In particular, the

33 Geostationary Environment Monitoring Spectrometer (GEMS), which was launched on

34 February 18, 2020, measures the total and tropospheric air pollutant columns hourly at spatial

35 resolutions of 7 km × 8 km for gas and 3.5 km × 8 km for aerosols (Kim et al., 2020), facilitating

36 the tracking of pollution transport from local to synoptic scales.

37   Recent studies have revealed the potential of satellite observations to evaluate surface air

38 quality, particularly in regions with sparse air quality-monitoring networks. The main approach

39 is to convert column density to surface concentrations using a shape factor of the ratio of the

40 partial column (Ω_{z_0}) within the lowest layer (z_0) to the total column (Ω_{total}) (Zhao *et al.*, 2019),

41 as follows:

42
$$\text{S} = \frac{\Omega_{z_0}}{\Omega_{\text{total}}} \times \frac{C}{\Delta z_o} \ ,$$

43 where S, C, and Δz_o are the surface concentration, column density, and lowest layer thickness,

44 respectively. Acquiring accurate profile shape information is critical for determining the

45 relationship between the column amount and surface concentration because the shape factor is

46 spatiotemporally variable. Considering this, numerous studies have obtained close

47 relationships using chemical transport model simulations, aircraft *in situ* measurements, and

48 satellite observations with high correlation coefficients (R) of 0.7 or more and used them to

49 scale up surface NO_2 to column NO_2 (Wang and Christopher, 2003; Boersma *et al.*, 2009;

50 Lamsal *et al.*, 2010). This strong correlation can be explained by the generally uniform

51 planetary boundary layer height (PBLH), and by aerosol type and abundance, which is also the

52 case for trace gases.

53   By contrast, the implications of weak correlations between column and surface

54 measurements remain unclear. Engel-Cox *et al.* (2004) found a negative correlation of AOD

55 and surface $PM_{2.5}$ in northwestern USA, and explained it based on elevated haze decoupled

3

56   from the surface. Thompson *et al.* (2019) examined weak correlations between Pandora column

57   (PC) measurements and surface *in situ* (SI) observations of NO_2 over the Yellow Sea during

58   the Korea–US air quality (KORUS-AQ) field study, and suggested, as a possible reason, the

59   transported non-uniform plumes originated in China and Seoul hundreds of meters above the

60   ground from the surface layer. The estimated surface $PM_{2.5}$ concentration was weakly

61   correlated ($R = 0.4$–0.49) with observed $PM_{2.5}$ concentrations in Seoul, because only PBLH

62   was added to the multi-linear regression model to correlate AOD to surface $PM_{2.5}$ (Kim *et al.*,

63   2021). This effect may be related to the significant impact of long-range transport on $PM_{2.5}$,

64   with a contribution of up to 39% in Seoul (Lee *et al.*, 2021). Thus, the wide variability in the

65   degree of correlation between PC-PM and SI-PM is closely related to vertical profile variability

66   (Flynn *et al.*, 2016).

67   It appears highly probable that several factors are responsible for the correlations between

68   PC-NO_2 and SI-NO_2; therefore, it is necessary to improve our understanding of the degree of

69   correlation through detailed measurements, including column concentration. In this study, we

70   focused on the impact of meteorology and chemistry on correlation variability using PC, SI

71   and aircraft measurements, as well as meteorological observations. Understanding vertical

72   profile variability is also useful for evaluating the effects of various emissions on urban air

73   quality, particularly in areas neighboring active large point source (LPS) emissions sites.

74   Quantifying the impact of LPS emissions on downwind cities remains challenging due to the

75   lack of three-dimensional (3D) measurements. Accurate vertical profile data are also useful for

76   improving remote sensing retrieval algorithms, because the profile shape contributes to the

77   conversion of slant column density into vertical column density as part of the air mass factor.

78   In mid-2019, the Pandonia Global Network (PGN; https://pandonia-global-network.org) was

79   launched, with support from the National Aeronautics and Space Administration (NASA) and

80   European Space Agency (ESA), to facilitate the validation and verification of low-orbit or

geostationary environmental satellites. This network is attempting to expand air quality

monitoring through integration with existing long-term air quality monitoring stations. Since

2020, the National Institute of Environmental Research, Economic and Social Commission for

Asia and the Pacific, and Korea Environment Corporation have been extending the Pandora

Asia Network to include 13 Asian countries, with support from the Korea International

Cooperation Agency. The Pandora Asia Network is expected to be widely used to study urban

air quality in Asia, which is increasingly deteriorating due to rapid economic growth.

As part of the GEMS Map of Air Pollution (GMAP) campaign, a suite of Pandora

instruments was deployed in Seosan, a South Korean coastal city, from November 2020 to

January 2021 (GMAP-2020), and we applied GMAP-2020 measurements to explore the

synergy of PC observations when evaluating air quality over Seosan. Further results from this

research project are also reported in this special issue, including GEMS validation and urban

air quality evaluations based on Pandora, aircraft, surface flux, and *in situ* surface chemical

measurements conducted during GMAP-2020.

2. GMAP-2020 campaign

GEMS was launched on February 19, 2020; it is the first instrument to observe air quality from

a geostationary Earth orbit. GEMS provides hourly air quality data on aerosols and gases at a

spatial resolution of 7 km × 8 km. It is a scanning ultraviolet (UV)-visible spectrometer that

observes key atmospheric constituents including O_3, NO_2, CO, SO_2, CH_2O, CHOCHO,

aerosols, clouds, and UV indices. This mission heralded a new era of satellite air quality

monitoring and will be joined by NASA's Tropospheric Emissions: Monitoring of Pollution

(TEMPO) and ESA's Sentinel-4 to form the GEO Air Quality Constellation in ~3 years, to

cover the most polluted region in the Northern Hemisphere.

During GMAP-2020, Pandora instruments (PA_1–PA_4) were deployed near large point

5

106   sources (LPS$_1$–LPS$_4$) in Seosan; *in situ* surface air quality monitoring systems (AQM$_1$–AQM$_6$)

107   and meteorological observations (Met$_1$–Met$_3$) were also used in this study (see their locations

108   in Fig. 1). Aircraft measurements were also used to validate GEMS and diagnose LPSs located

109   in industrial areas surrounding Seosan. We explored the synergy of Pandora observations and

110   SI measurements, based on measurements collected during GMAP-2020, by evaluating air

111   quality in industrial Seosan (where LPSs are densely clustered). We particularly investigated

112   the impacts of vertical profile and sub-pixel variability for trace gases and aerosols, for further

113   GEMS validation. All measurement sites for both GMAP-2020 campaigns are indicated in

114   Figure 1.

115

116   **3. Methods**

117   **3.1 Study area**

118   Seosan, the target area of the GMAP-2020 campaign, is a small city with a population of

119   174,780 in 2017; it is accessed via three expressways to the east and four national highways

120   cross the city. It is located in midwestern South Korea, and is affected by >300 emissions point

121   sources including LPSs. Coal-fired power plants including Taean, Dangjin, the Hyundai

122   Dangjin steelworks, and the Daesan petrochemistry industrial complex (LPS$_1$–LPS$_4$,

123   respectively, in Fig. 1) have the highest emissions rates in South Korea. The Hyundai Dangjin

124   steelworks (LPS$_3$) and Taean and Dangjin power plants (LPS$_1$ and LPS$_2$) emit 10.5, 11, and

125   8.8 Gg of NOx per year, respectively. Although Seosan accounts for only 1.8% of the

126   population of Seoul, its NOx emissions (10.2 Gg year^{-1}) account for 13.2% of its total NOx

127   emissions. The transportation sector of Seosan is a far greater NOx source than the industrial

128   sector of Seoul (ratio of 99:1); however, within Seosan, the industrial sector is on par with the

129   transport sector (52:48; http://airemiss.nier.go.kr).

130   During the past decade, the annual mean NO$_2$ level in Seosan has been 17 ppb, which is

6

131 approximately half of that in Seoul (31.2 ppb). NO_2 exhibits strong seasonal variation, reaching

132 a minimum in summer and maximum in winter, due to meteorological factors and greater

133 energy use during winter (Kim and Kim, 2020). Therefore, the timing of the GMAP-2020

134 campaign was well suited to tracking pollution.

135

136 **3.2 Pandora measurements**

137 Pandora measures the UV and visible wavelengths (280–525 nm) of direct sunlight with a

138 spectral resolution of 0.6 nm, to determine the vertical column density of NO_2, O_3, and HCHO

139 (Herman *et al.*, 2009). For measurements in Dobson units (DU; 1 DU = 26.9 Pmol cm^{-2}),

140 column NO_2 has a very high signal-to-noise ratio (700:1) and very high precision (0.01 DU)

141 for clear skies (Herman *et al.*, 2009). The vertical column density of NO_2 can be determined

142 using DOAS software (Van Roozendael and Fayt, 2001). Pandora direct-sun measurements are

143 advantageous in that the air mass factor is simplified, and therefore is dependent only on the

144 geography for a known solar zenith angle.

145   From retrieved Pandora measurements, tropospheric and total (=tropospheric +

146 stratospheric) vertical column densities are both available. However, it should be noted that

147 appreciable uncertainties cannot be neglected in the tropospheric NO_2 profiles obtained from

148 Pandora instruments, particularly for the high aerosol-loading areas such as East Asia. In this

149 background, we used total vertical column densities in the present study, and also confirmed

150 that they have a high correlation with the tropospheric column densities observed in our study

151 period with little change in stratospheric column density in space and time at the local scale.

152   Four Pandora instruments were installed at sites to the south of LPSs (Fig. 1) during the

153 GMAP-2020 campaign, i.e., at Seosan Daehoji, Seosan Dongmun, Seosan City Council, and

154 Seosan Super Site (PA_1–PA_4 in Fig. 1). The presence of clouds reduces vertical column density

155 precision by decreasing the number of photons arriving at Pandora instruments within a fixed

156 integration time. Therefore, the retrieved Pandora measurements were cloud-screened using an

157 observed cloud cover of 0.6. Cloud cover was provided by the Korea Meteorological

158 Administration (KMA), and the precision improvement afforded by cloud screening was

159 verified by comparing each Pandora-derived vertical column density with the median vertical

160 column density, with and without cloud screening within the inter-comparison period.

161   At PA_4, the operating period was extended to cover almost the entire year (November 12,

162 2020–October 30, 2021) including the GMAP-2020 campaign period, and the Pandora spectra

163 were processed into vertical column density data for trace gases using the standard NO_2

164 algorithm in BlickP software provided by PGN (Cede, 2019). The resultant PC-NO_2 data were

165 obtained from the PGN website (https://pandonia-global-network.org) for the 1-year period

166 from Nov. 12, 2020 to Oct. 30, 2021, and were also used as PC-NO_2 statistics for PA_4, in this

167 study.

168

169 **3.3 Surface and airborne chemical measurements**

170 Hourly average data for SI-NO_2 over a period of 1 year were obtained from Ministry of

171 Environment AQM network stations in Seosan: Pandori, Leewon, Taean, Dongmoon,

172 Seongyeon, and Daesan (AQM_1–AQM_6, respectively, in Fig. 1). The Seosan Super Site

173 (PA_4/AQM_1) provided hourly data for NO and NOy via an NO-DIF-NOy analyzer (42i-Y;

174 Thermo Scientific, Waltham, MA, USA), and for $PM_{2.5}$ chemical species using an ambient ion

175 monitor (AIM; URG 9000D, URG Corp., Chapel Hill, NC, USA). Weekly zero and span

176 checks were conducted for NOy calibration, to ensure that differences between checks

177 remained <3%. Water-soluble ions in aerosol and gaseous species were measured hourly using

178 an AIM, and ion mass balance was used to ensure data quality under the quality control

179 procedures of the AQM network installation and operation guidelines (NIER, 2021).

180   Aircraft measurements were conducted during the GMAP-2020 campaign period, and

181   nine flights were conducted on 8 days (Nov. 26, 27, and 28 and Dec. 1, 6, 8, 9, and 12, 2020).

182   The horizontal and vertical distributions of NO_2 and O_3 over Seosan were measured during

183   GMAP-2020 using an NO_2 monitor (T500U; Teledyne, Thousand Oaks, CA, USA) and an O_3

184   analyzer (TEI49C; Thermo Scientific) onboard the Cessna Grand Caravan 208 B. These

185   instruments had response times of <40 and <20 s, and detection limits of 40 ppt and 1 ppb,

186   respectively. The flight paths included a raster mode over all of Seosan at a height of 500–700

187   m and a profiling mode from 500 m to 1.5 km over PA_1 and PA_4 (Fig. 2).

188

189   **3.4 Meteorological measurements**

190   Ground-based hourly observation data for meteorological variables were obtained from Seosan

191   Automated Synoptic Observing System (ASOS) stations maintained by the KMA, and wind

192   and temperature profile data were obtained twice daily (0000 and 1200 UTC) via a rawinsonde

193   instrument at the Osan World Meteorological Organization upper air measurement station

194   (47122) near Seosan. Due to time constraints of the sonde measurements, information on PBLH

195   variation was obtained from Unified Model (UM) simulation results provided on the KMA

196   website (https://afso.kma.go.kr).

197   During the GMAP-2020 campaign, a 3D sonic anemometer (CPEC200; Campbell

198   Scientific, Logan, UT, USA) was also installed on the rooftop at PA_4 for turbulent flux

199   measurements at the city–atmosphere interface (Hong *et al.*, 2019). All wind components and

200   sonic temperatures were measured at a 10 Hz sampling rate, and ground-level sensitive heat

201   flux was measured directly using a 30 min averaging period. Quality controls such as double

202   rotation, spike removal, and outlier filtering were also applied.

203

204   **3.5 Correlation analyses**

205   We examined the synergy of PC and SI data obtained during the GMAP-2020 campaign, and

206 combined these measurement data to evaluate air quality in Seosan, South Korea. We attempted

207 to interpret the meteorological and photochemistry data measured during GMAP-2020, and to

208 demonstrate that caution is required when attempting to study the vertical structure of air

209 pollutants using either surface observations or satellite data only, particularly in industrial

210 areas.

211 First, we examined the combined use of year-long PC-NO_2 and SI-NO_2

212 measurements, and investigated the factors modulating their correlation. Numerous studies

213 have examined the correlations between chemical species, including aerosols (Thomspon et

214 al., 2019; Wang et al., 2019; Kim et al, 2012; Jo et al., 2013; Sanchez et al., 1990; Kim et al,

215 2018). Wang *et al.* (2019) reported that aerosols moderately correlate with NO_2 due to the

216 frequent occurrence of lifted layers probably related to the transport of pollutants. Jo *et al.*

217 (2013) differentiated haze types using the trajectory speed and direction and different synoptic

218 conditions. In this background, we hypothesized that their differences in PC-NO_2 and SI-NO_2

219 were due to meteorological conditions, and performed k-means and agglomerative hierarchical

220 cluster analyses of various meteorological variables. Clustering is the grouping of objects that

221 are alike and are different from the objects belonging to other clusters. As a first step, k-means

222 Clustering was applied to find smaller clusters until each object was classified in one cluster.

223 Subsequently, agglomerative hierarchical steps are applied to make up for the shortcomings of

224 k-means clustering, in which once merging (or splitting) is done, it can never be undone. More

225 details are found in Venkat Reddy *et al.* (2017). We used XLSTAT software (Addinsoft, Paris,

226 France) for the cluster analysis with eight meteorological variables representing local and

227 synoptic circulations in the cluster analysis: surface wind speed (Wsfc), 925 hPa temperature

228 (T925), sea level pressure (Psfc), pressure tendency (dPsfc/dt), 850 hPa wind speed (W850)

229 and its north–south and east–west components (NS850 and EW850), and 500 hPa geopotential

230 height (GPH500). We subtracted 30-day moving averages from all data to account for typical

10

231 seasonal variation. Monthly averages were used for PC-NO$_2$ analysis due to the limited

232 availability of hourly data.

233 Correlations between PC-NO$_2$ and SI-NO$_2$ were analyzed in each meteorological group

234 and the impact of photochemistry was interpreted based on case-specific features. We also

235 investigated correlations in association with near-surface micrometeorological variables such

236 as PBLH in each meteorological group.

237

238 **4. Results and Discussion**

239

240 **4.1 Correlation analysis results for PC-NO$_2$ and SI-NO$_2$**

241 The yearly PC-NO$_2$ statistics at four Pandora sites (PA$_1$–PA$_4$) are summarized in Table 1. The

242 total averaged PC–NO$_2$ over all sites was 0.45 DU during GMAP-2020, which is well above

243 the typical values (0.1–0.2 DU) for Anmyeondo (the location is shown in Figure 1), a

244 representative background site (Herman *et al.*, 2018). Although site PA$_3$ is located in a rural

245 area, it nevertheless exhibited the highest PC-NO$_2$ amounts, suggesting that plumes were

246 frequently transported from nearby point sources and/or urban areas.

247 Scatter diagrams of hourly PC-NO$_2$ and SI-NO$_2$ measurements from Pandora sites PA$_1$–

248 PA$_3$ (GMAP-2020) and PA$_4$ (yearly measurement; November 12, 2020–October 30, 2021) are

249 shown in Fig. 3a. These hourly data had a fair 1:1 linear relationship ($R = 0.41$), implying the

250 overall uniformity of NO$_2$ profiles, whereas the linear relationship with PC-NO$_2$ weakened as

251 SI-NO$_2$ levels increased (Fig. 3a). It appears that the SI-NO$_2$ has a distinct diurnal change

252 despite the same PC-NO$_2$, and higher variable surface NO$_2$ levels may result from the relatively

253 weaker linear relationship between PC-NO$_2$ and SI-NO$_2$. To explore these anti-correlation

254 cases further, we selected the lower and upper bounds of the tendencies; these are plotted in

255 Fig. 3b, which shows that PC-NO$_2$ was positively correlated with SI-NO$_2$ on February 24, 2021

256 (R = 0.88), while a negative correlation occurred on April 21, 2021 (R = –0.88), indicating a

257 wide range of case-specific correlations. The negative correlation on April 21 (Fig. 3b) implied

258 that the nonhomogeneous NO_2 distributions vertically were partially due to the photochemical

259 process. For example, the decrease in PC-NO_2 despite an increase in SI-NO_2 might have

260 occurred because NO_2 is removed by photochemical loss; it can occur more severely in the

261 upper atmosphere with high OH concentrations. Another possible reason is the occurrence of

262 lifted layers related to pollutant transport, yielding sharp changes in vertical concentration from

263 the surface to the upper layer. The case-specific discussion follows.

264

265 **4.2 Impacts of meteorological conditions on correlations between PC-NO_2 and SI-NO_2**

266 Our k-means cluster analysis distinguished three groups with the lowest within-group variance

267 and largest among-group variance. Among the total of 141 cases, 47, 66, and 28 were classified

268 into groups 1–3, respectively. Thus, group 2 had the largest proportion of cases (47%) and

269 group 3 had the smallest (20%). The combination of meteorological components in group 1

270 indicated the end of a high-pressure system (Psfc > 0, dPsfc/dt < 0), with southerly winds

271 (NS850 > 0) bringing warmer air (T925 > 0) to the region, leading to stable atmospheric

272 stratification and weak surface winds (Fig. 4). This group 1 meteorological mode appeared to

273 result in very weak NO_2 ventilation, which produced the highest PC-NO_2 and SI-NO_2 values.

274 Group 3 showed the opposite trend, with strong northerly winds bringing colder air into the

275 region, leading to an unstable atmosphere and stronger surface winds, and ultimately

276 decreasing PC-NO_2 and SI-NO_2 to their lowest levels.

277 SI-NO_2 was approximately twice as high in group 1 than group 3, whereas PC-NO_2

278 showed no significant difference (Fig. 4a). We hypothesized that PBLH might also differ

279 significantly under these micrometeorological conditions; therefore, we further explored daily

280 maximum PBLH simulated by the Global Forecast System (GFS) and Lagrangian backward

12

281 trajectories obtained from Hybrid Single-Particle Lagrangian Integrated Trajectory

282 (HYSPLIT) and GFS system for the 141 cases. The mean simulated PBLH in Seosan, our study

283 area, was 942.1 ± 405.3 m for 2020, which was similar to the annual mean daily maximum

284 PBLH (1,013.6 m) in Osan (Lee *et al.*, 2013). However, the simulated PBLH differed

285 significantly among the three groups (767.0 ± 304.8, 923.2 ± 335.3, and $1,280.6 \pm 501.2$ m for

286 groups 1–3, respectively). The PBLH for group 3 was 1.7-fold higher than that for group 1

287 (Fig. 4k). We also detected significant differences among the three groups in synoptic

288 components of the lower troposphere including W850, as well as in local meteorological

289 parameters such as the sea breeze index (SBI) suggested by Biggs and Graves (1962), which

290 is defined as, $\text{SBI} = \dfrac{U^2}{C_p \Delta T}$, where U is Wsfc (Fig. 4c), C_p is specific heat, and ΔT is the

291 temperature difference between T925 and the sea surface temperature. Thus, the SBI represents

292 the ratio between inertial ($\rho U^2/2$) and buoyance forces ($\rho g C_p \Delta T$), where ρ is air density and g

293 is gravity, and its value provides an indication of the likelihood of local circulation events such

294 as sea breezes; at higher SBIs (i.e., SBI > 3), sea breezes cannot overcome the prevailing wind,

295 whereas lower SBIs (i.e., 0 < SBI < 3) can indicate strong sea breezes.

296   In the example shown in Fig. 4l, the SBI for groups 1–3 was 0.1 ± 4.5, 0.1 ± 9.2, and -0.2

297 $\pm$ 12.5, respectively. Most SBIs in group 1 ranged from 0 to 3, indicating that group 1

298 corresponded to the dominant local circulation (LD), whereas the SBIs in group 3 had the

299 lowest frequencies comparing 1 and 3, which corresponded to a dominant synoptic-scale

300 circulation (SD). Group 2 can be considered a mixture of local and synoptic-scale circulation

301 (MD). These results indicate that Seosan may experience frequent LD conditions (with sun on

302 one third of the days of the year), with infrequent SD conditions (one fifth of all days).

303

304 **4.2.1 Relationship between daily mean PC-NO₂ and SI-NO₂ under LD, MD, and SD**

conditions

Scatter diagrams of daytime mean PC-NO$_2$ and SI-NO$_2$ measurements at Seosan over the entire

1-year period are shown in Fig. 5. Based on the 141 cases, daytime mean values averaged

between 1100 and 1700 KST were used to reduce the effect of nocturnal PBLH variation. Other

data selection criteria included concurrent PC-NO$_2$ and SI-NO$_2$ measurements, with data

acquisition rates of >80% per day. Overall, PC-NO$_2$ and SI-NO$_2$ were strongly correlated ($R =$

0.73; Fig. 5), suggesting that the vertical profiles were generally uniform in the PBL throughout

all four seasons. The slope of the linear regression curve shown in Fig. 5a was 0.02 DU/ppb (=

0.53×10^{15} molecules cm^{-2}/ppb), which is comparable to values (0.3–0.59×10^{15} molecules

cm^{-2}/ppb) obtained previously in a study of surface and OMI-NO$_2$ measurements downwind

of strong point sources in Israeli cities (Boersma *et al.*, 2009). The intercept (0.17 DU) was

within the range of previous Anmyeondo Pandora measurements, suggesting that intercepts of

0.15–0.2 DU may represent the local background PC-NO$_2$ amount (including the stratospheric

NO$_2$), rather than the influence of local anthropogenic NO$_2$ emissions.

We classified daily averaged PC-NO$_2$ and SI-NO$_2$ data according to the three

meteorological conditions (LD, MD, and SD) and detected a weak correlation under LD

conditions (Fig. 5b); the lowest coefficient of determination for the LD condition ($R^2 = 0.34$)

was approximately half of those for the MD (0.359) and SD (0.64) conditions, suggesting that

NO$_2$ vertical profiles were more complex under LD conditions, with anomalous layers.

4.2.2 Diurnal variation in column-surface NO$_2$ under LD, MD, and SD conditions

Diurnal patterns of PC-NO$_2$, SI-NO$_2$, and O$_3$ under SD, MD, and LD conditions are shown in

Fig. 6. Under LD conditions, PC-NO$_2$ increased from morning to afternoon (Fig. 6a), whereas

under SD conditions, it had a weak morning peak and subsequent decrease until late afternoon

(Fig. 6c). Under MD conditions, PC-NO$_2$ had one large peak in the morning and a shoulder

14

330   peak in the late afternoon (Fig. 6b). However, SI-NO$_2$ showed nearly identical diurnal patterns

331   among the three meteorological conditions, with an early morning peak followed by a second

332   peak in the late afternoon (Fig. 6d–f). Diurnal patterns of O$_3$ were strongly associated with O$_3$-

333   NO$_2$ photochemical reactions under both LD and MD conditions (Fig. 6g–h), whereas no

334   particular photochemical effects were detected under SD conditions (Fig. 6i).

335   A simple linear regression was applied to daytime average (1100–1700 LST)

336   measurements of both PC-NO$_2$ and SI-NO$_2$ under the three meteorological conditions, and

337   yielded correlation coefficients (R) of 0.51 and 0.41 for SD and MD conditions, respectively;

338   however, LD conditions produced a significantly lower R (0.27). Thus, under SD conditions,

339   strong synoptic winds suppressed PC-NO$_2$ and SI-NO$_2$ diurnal fluctuations, rendering them

340   similar to each other. Strong winds also inhibited local effects of O$_3$ formation on the diurnal

341   variation in PC-NO$_2$, and the smaller impact of chemical conversion from local NO$_2$ to O$_3$

342   lowered R values during the day. Under MD conditions, both PC-NO$_2$ and SI-NO$_2$ exhibited

343   distinctive peaks in the morning with a degree of time lag; both subsequently declined toward

344   noon, and showed higher R values than those obtained under SD conditions. By contrast, under

345   MD conditions, correlations were enhanced due to a minimum around 1500 KST for both PC-

346   NO$_2$ and SI-NO$_2$, despite time lags in both peaks in the morning and afternoon.

347   Previous studies of the Megacity Air Pollution Seoul (MAPS-Seoul) and KORUS-AQ

348   campaigns reported a typical pattern of continuously increasing PC-NO$_2$ over the Seoul

349   metropolitan area (Chong *et al.*, 2018; Herman *et. al.*, 2018). However, in the current

350   campaign, we found similar results only under LD conditions. The diurnal patterns reported in

351   previous studies were mainly caused by the dominance of NO$_2$ emissions sources over NO$_2$

352   losses (Chong *et al.*, 2018; Herman *et al.*, 2018) among several processes associated with NO$_2$

353   photochemical loss, including transport and deposition, which were also investigated in

354   specific cases in the current study.

355   In this study, we extended the correlation analysis, and investigated the correlation

356   between hourly PC-NO$_2$ and SI-NO$_2$ data. The results show a lower correlation in the morning,

357   and a higher correlation in the afternoon (Fig. S1). The respective median correlation

358   coefficients for the LD, MD, and SD meteorological conditions were -0.71, 0.18, and 0.22 in

359   the morning (0900–1200 LST), and 0.84, 0.77, and 0.79 in the afternoon (1200–1400 LST).

360   These values may reflect PBL development. SI-NO$_2$ decreases in the morning due to the rapid

361   growth of the PBL, while PC-NO$_2$ increases due to the accumulation of NO$_2$ in the atmosphere,

362   deriving a lower correlation. However, there is very little change in the PBL in the afternoon,

363   and PC-NO$_2$ and SI-NO$_2$ show similar changes, yielding a positive correlation each other

364   during the GMAP-2020 campaign.

365

366   **4.3 Aircraft measurements collected during GMAP-2020**

367   Data collected via aircraft during GMAP-2020 are summarized in Table 2. A total of nine

368   aircraft measurements were conducted during the campaign period (November 12, 2020–

369   January 20, 2021). Four of nine flights were conducted under LD conditions, and the remaining

370   flights (except that on November 27, 2020) were conducted under MD conditions. No aircraft

371   measurements were consistent with SD conditions during the GMAP-2020 campaign.

372   We examined spiral segments from each flight over Seosan during 1100–1700KST to

373   exclude marginal effects of diurnal variation in NO$_2$ (Fig. 2). The overall results indicated that

374   the vertical O$_3$ profiles were relatively constant in the PBL, whereas NO$_2$ profiles appeared to

375   be highly dependent on meteorological conditions. We compared data collected during flights

376   conducted under LD (one flight) and MD conditions (two flights) during the GMAP-2020

377   campaign, to examine differences in the vertical structures of the PA and SI observations.

378   Aircraft measurements of vertical NO$_2$ and O$_3$ profiles for flights FL-5 (December 6) and FL-

379   6 (December 8) under LD conditions are shown in Fig. 7, along with 24 h backward trajectories

380   starting at different altitudes (100, 500, and 1,000 m). All observed NO_2 profiles shown in Fig.

381   7 appeared to have generally exponential curves, with anomalous features at higher altitudes.

382   For example, when vertical turbulent mixing prevailed within the PBL (O_3 profile, Fig. 7b),

383   the data were fitted with an exponential vertical curve, and the anomalous NO_2 layer aloft was

384   found to have a height of 1.5 km, which was higher than the estimated PBLH of 1.2 km.

385   HYSPLIT 24 h backward trajectories starting at 1200 KST showed that all air mass from the

386   surface to the lower free atmosphere was transported over the Yellow Sea via the Shandong

387   Peninsula (Fig. 7c). This finding suggests that the anomalous NO_2 layer aloft was not produced

388   locally (i.e., from local LPS emissions), but instead traveled via long-range regional-scale

389   transport. This transport of NO_2 across the region was also discussed and might be particularly

390   high during the winter when the NO_x lifetime is relatively longer (Stohl *et al.*, 2002; Wenig *et*

391   *al.*, 2003; Lee *et al.*, 2013). According to Anmyeondo Lidar measurements for December 6

392   (http://kalion.kr), the anomalous NO_2 layer aloft corresponded well to an aerosol layer that

393   appeared at ~1.0 km at approximately 1200 KST, persisting until 2200 KST. However, based

394   on a cross-comparison of our data, high surface levels of SI-NO_2 (> ~4 ppb; Fig. 7a) were

395   influenced more by local LPS than by that in the atmosphere aloft due to long-range transport

396   (Fig. 7a).

397   Aircraft measurements for flight FL-7 (December 9) under LD conditions are shown in

398   Fig. 7b. The NO_2 vertical profile exhibited an exponential curve, with an anomalous peak at

399   ~600 m immediately above the top of the simulated PBL. HYSPLIT backward trajectory data

400   starting at 1200 KST showed that the non-surface air had a different origin from the surface air

401   (Fig. 6d), indicating that the anomalous NO_2 plume likely traveled from coal-fired power plants

402   in a nearby industrial city (Taean) northwest of Seosan. This finding indicates a distinct vertical

403   structure of higher NO_2 at the surface due to strong local emissions, whereas lower NO_2 levels

404   were observed at higher altitudes, with anomalously high NO_2 levels in some layers aloft due

17

405   to medium-range transport from nearby areas. Thus, despite the limited number of aircraft

406   measurements, the elevated anomalous NO_2 structure that was observed intermittently led to a

407   negative correlation between PA-NO_2 and SI-NO_2. The discrepancies imply that vertical

408   profile distribution study should proceed cautiously when only surface measurements are

409   obtained under LD meteorological conditions.

410   Aircraft measurements were conducted under MD conditions on flights FL-1 (November

411   26), FL-3 (November 28), and FL-8 (December 12) (Fig. 8). We applied several regression

412   models (linear, exponential, and polynomial) to three vertical structures, and obtained two

413   distinct NO_2 vertical profile patterns from the surface to the PBLH: decreasing linearly for FL-

414   1 and FL-8 (Fig. 8), and constant with altitude for FL-3 (Fig. 8b). None of the three cases

415   showed anomalous layers above the PBLH, similar to the exponentially declining profiles

416   obtained under LD conditions (Fig. 7). These vertical structures observed under MD conditions

417   may have been induced by strong vertical mixing within the PBL, supplemented by prominent

418   surface photochemical losses at the same time. The vertical O_3 profile during FL-1 showed a

419   decoupled structure, with different patterns within and above the PBL (Fig. 8d); however, the

420   other 2 days showed uniform distributions, with no particular anomalous features between the

421   upper PBL and surface atmosphere (Fig. 8b, c, e, f). The observed daily maximum sensible

422   heat fluxes measured at Seosan (Fig. S3) were much higher for FL-3 (175.9 Wm^{-2}) than FL-1

423   and FL-8 (118.9 and 102.0 Wm^{-2}), suggesting that vertical turbulent mixing was much more

424   prominent during FL-3. These chemical and physical characteristics are all related to MD

425   conditions. Thus, the higher coefficient of determination ($R^2 = 0.64$) obtained under MD

426   conditions (Fig. 5b) has an important bearing on the absence of irregular or anomalous layers

427   aloft, with little variation regardless of the shape of the curve (Figs. 7 and 8).

428

429   **4.4 Analyses of column–surface relationships for specific GMAP-2020 cases**

18

430 Figure 9 shows examples of PC-NO$_2$ and SI-NO$_2$ diurnal variation under LD (FL-5 and FL-7)

431 and MD (FL-1 and FL-8) conditions, and Fig. 10 shows latitudinal mean distributions for FL-

432 5 and FL-7, based on the aircraft measurement data shown in Figs. 7 and 8. PC-NO$_2$ was

433 decoupled from SI-NO$_2$ on 2 days, FL-5 and FL-7, which were both classified as having LD

434 conditions (Fig. 9a, b), whereas good vertical mixing and uniform NO$_2$ distribution were

435 observed on the remaining 2 days, FL-1 and FL-8, which showed MD conditions (Fig. 9c, d).

436 According to our analysis of the aircraft measurements (Fig. 7), the poor correlations between

437 PC-NO$_2$ and SI-NO$_2$ captured by FL-5 and FL-7 were mainly due to an NO$_2$ polluted layer

438 transported aloft, as described in Section 4.3.

439

440 **4.4.1 LD conditions**

441 Several cases showed poor correlations between PC-NO$_2$ and SI-NO$_2$ under LD conditions

442 within the study period. When we examined the results of previous studies (Thompson et al.,

443 2019; Chong et al., 2018; Herman et al., 2018; Kim et al., 2021), we first considered the

444 possibility that LPS emissions influenced downwind regions under LD conditions, because the

445 increase in PC-NO$_2$, but not SI-NO$_2$, may have required an additional source of NO$_2$ apart from

446 early afternoon traffic emissions. The FL-5 data for December 6 represent an example of this,

447 showing a poor correlation between PC-NO$_2$ and SI-NO$_2$ ($R^2 = 0.06$; Fig. 9a). On the same day,

448 Anmyeondo LIDAR detected two elevated aerosol layers at 1200 and 1600–2200 KST

449 (http://kalion.kr); the first aerosol layer may reflect a PC-NO$_2$ peak, as shown in Fig. 9a. The

450 HYSPLIT backward trajectories, starting at different altitudes from the surface to the lower

451 troposphere, revealed that all air parcels moved eastward from China to Anmyeondo and

452 Seosan (Figure 1); thus, other NO$_2$ plumes may have begun to pass over Seosan at 1600KST

453 (Fig. 7c). Longitudinal SI-NO$_2$ distributions (Fig. 10) exhibited 5.2 ppb at 126.1°E, 8.1 ppb at

454 126.3°E, and 7.3 ppb at 126.4°E, averaged between 1300 and 1600 KST by longitude (Table

455   S1), whereas they were nearly constant at a height of 500–600 m on December 6. Therefore,

456   westerly winds advected cleaner air from Padori (AQM$_1$) to Seosan at the surface, but not at a

457   height of 500–600 m, contributing to low SI-NO$_2$ levels in the afternoon (Fig. 9a).

458   Another example of a weak correlation was obtained by flight FL-7 (December 9), as

459   shown in Fig. 9b. Time series PC-NO$_2$ data exhibited several peaks during 1200–1400 KST

460   (Fig. 9b), whereas SI-NO$_2$ showed less temporal variation, resulting in a weak correlation (R =

461   –0.24) compared to the overall daytime (1100–1700 KST) correlation (R^2 = 0.53; Fig. 5a).

462   Latitudinal NO$_2$ levels at high altitudes of ~600 m (Fig. 10b) gradually increased northward,

463   whereas surface NO$_2$ was minimal at the midpoint. For example, at high altitudes, the

464   latitudinal mean NO$_2$ levels were 1.4 ppb (36.8°N), 4.1 ppb (36.9°N), and 5.1 ppb (37.0°N),

465   whereas the SI-NO$_2$ levels at the same sites were 18.0 ppb (36.8°N), 14.3 ppb (36.9°N), and

466   16.8 ppb (37.0°N), respectively, averaged during 1200–1400 KST by latitude (Table S1). This

467   finding is attributable to a prevailing north wind that transported NO$_2$ southward at high

468   altitudes, while simultaneously ventilating SI-NO$_2$ toward outer Seosan, resulting in the

469   development of several PC-NO$_2$ peaks. By contrast, SI-NO$_2$ decreased slowly (Figs. 9b and

470   10b).

471

472   **4.4.2 MD and SD conditions**

473   We obtained higher PC–SI correlation coefficients under MD and SD conditions than LD

474   conditions (Figs. 5b and 9c, d). Under MD and SD conditions, diurnal variation in PC-NO$_2$ and

475   SI-NO$_2$ showed simultaneous declines from early morning until noon (Fig. 6). Notably, PC-

476   NO$_2$ showed a continuously decreasing trend, particularly during the morning hours, in the

477   period of approximately 0900–1200 KST under both MD and SD conditions (Fig. 6b, c). These

478   diurnal patterns of decreasing PC-NO$_2$ in the study area were opposite to those reported in

479   previous studies (Chong *et al.*, 2018; Herman *et al.*, 2018) that observed increasing PC-NO$_2$ in

large urban areas during the daytime, caused by higher NO_2 emissions even during

photochemical NO_2 losses to form O_3.

We hypothesized that decreasing PC-NO_2 can occur due to photochemical loss and

surface wind transport, which both intensify with increasing solar radiation in the morning.

Photochemically, NO_2 is converted into photochemical oxidants such as PAN, HNO_3, and

nitrate under sunlight, thereby disrupting the NOx–VOC–O_3 cycle. Concurrently, Wsfc

intensified due to thermal turbulence transport of NO_2 emissions away from Seosan during the

day. Thus, PC-NO_2 decreases under MD conditions as a result of ventilation effects caused by

stronger wind speeds. There are two possible mechanisms for this: sea breeze penetration

(because the study area is adjacent to the northern coast of the Taean Peninsula; Fig. 1) and

vigorous turbulent mixing (which leads to vertical mixing of surface NO_2 during PBL growth;

Sun *et al.*, 2013). We investigated these factors in detail for specific cases.

Figure 11 shows the diurnal variation in selected meteorological and chemical variables

measured under MD (November 25) and SD conditions (December 14). Under MD conditions

(Fig. 11a–c), declines in PC-NO_2 and SI-NO_2 were observed toward noon. In particular,

decreasing PC-NO_2 was accompanied by increased Wsfc (Fig. 11b); therefore, we examined

GMAP-2020 campaign measurements of sea breeze penetration. Figure S2a shows diurnal

variation in observed air temperatures at site Met_1 and measured sea surface temperatures at

nearby site Met_2 (37.14°N, 126.01°E), located 55 km from PA_4. The thermal meteorological

observations were used to calculate SBI (+0.37), which was greater than +3 (the threshold for

sea breeze occurrence; Brigges and Graves, 1962). Sea breeze disturbances with a sharp

decrease (increase) in temperature (humidity) were observed at site Met_3 (Fig. S3b), which is

located on the northern coastline of Taean Peninsula (Fig. 1). However, sea breezes did not

progress inland at the Met_1 Seosan Meteorological Automated Surface Observing System

(ASOS) site, which is closer to the Pandora sites; sea breezes did not correlate with NO_2

505   ventilation to offset its high emission.

506   We further detected a strong positive correlation between wind speed and sensible heat

507   flux (Fig. 11b). We speculated that thermal and momentum turbulences caused by a vertical

508   temperature gradient and surface friction entrained surface turbulence, thus increasing

509   momentum in the free atmosphere downward to the surface due to strong turbulent mixing

510   within the PBL, in turn leading to a uniform vertical NO_2 profile with a positive correlation

511   between PC-NO_2 and SI-NO_2. Figure S3 shows a comparison of daily maximum sensible heat

512   and momentum fluxes under LD, MD, and SD conditions during the GMAP-2020 campaign.

513   SD conditions showed the highest mean heat flux, followed by MD and LD, indicating that

514   downward momentum transport led by both heat and momentum fluxes plays a greater role in

515   Wsfc enhancement under MD than LD conditions within the PBL.

516   Photolytic NO_2 loss was detected as temporal variation in NO_2, NO_3^-, and CO at PA4.

517   Because no NO_2 analyzer was installed at PA4, $NO_2^*(= NO_y–NO)$ was used instead of NO_2

518   under the assumption that NO_z is negligible in winter. Figure 11c shows the diurnal variation

519   in NO_2, O_3, and NO_3^- under MD conditions, normalized by CO to reduce the effect of PBL

520   evolution. The results showed that NO_2/CO decreased after the morning peak; however, NO_3^-

521   /CO and O_3/CO increased toward midday, indicating that photolytic activity also contributed

522   considerably to the concurrent decline of SI-NO_2 and PC-NO_2 (Fig. 11a). In turn, this indicated

523   that photochemistry can contribute to higher correlation coefficients under MD conditions.

524   Under SD conditions (Fig. 11d–f), PA-NO_2 and SI-NO_2 exhibited weak diurnal variability

525   compared to LD and MD conditions. SD conditions on December 14 produced significantly

526   stronger winds (i.e., wind speed > 6 m s^{-1} at 1300 KST), with generally higher PBLHs (Fig.

527   11e). Meteorological features, such as strong wind at both 850 hPa (18.0 m s^{-1}) and 10 m height

528   (4.26 m s^{-1}), suppressed both PC-NO_2 and SI-NO_2 (7.3 ppb and 0.31 DU, respectively) to

529   below the average, producing a strong correlation ($R = 0.9$ at AQM5) and nearly flattening their

530   temporal curves during the day (Fig. 11d). Thus, under SD conditions, wind speed and

531   turbulent fluxes such as sensible heat flux had larger values, and NO_2 and NO_3^- decreased or

532   increased at the same time during the day (Fig. 11f), indicating that the transport effect was

533   much greater than that of local photochemical loss over the study area.

534   In conclusion, in this case-specific study, we assessed the correlations between PC-NO_2

535   and SI-NO_2, and explored their mechanisms by investigating the impact of meteorological and

536   photochemical conditions. A weak correlation between PC-NO_2 and SI-NO_2 occurred when

537   anomalously high concentrations remained, with ragged fragments of NO_2 plumes in the upper

538   or middle layers. We also found that a negative correlation occurred intermittently under LD

539   conditions, with generally lower PBLH. In particular, elevated pollutant levels due to regional-

540   scale transport or decoupled NO_2 plumes advected within the PBL may have also caused the

541   weak correlation between PC-NO_2 vs. SI-NO_2. These phenomena were detected only from the

542   PA–SI coupled measurements in this study. Thus, when either PC or SI observations are

543   applied alone for understanding the vertical structure of air pollutants, undetected bias can

544   occur under LD conditions, particularly where transport processes prevail, and these results

545   can be also applicable to GEMS observations analysis.

546

5. Conclusion

548 We explored the potential applicability of combined PC-NO_2 and SI-NO_2 measurements

549 collected at Seosan during the GMAP-2020 campaign. We characterized the correlation

550 between PC-NO_2 and SI-NO_2 under various conditions to understand the complex air quality

551 of Seosan, which appears to be vulnerable to LPS emissions from surrounding areas. We

552 hypothesize that correlations between PC-NO_2 and SI-NO_2 are closely related to NO_2 vertical

553 profiles, which also depend on meteorological conditions. We performed statistical analyses of

554 a year-long PC-NO_2 dataset (November 12, 2020–October 30, 2021) combined with

555   meteorological data, *in situ* ground data, and airborne chemical data measured during the

556   GMAP-2020 campaign in the same period.

557   Our results show that hourly $PC-NO_2$ and $SI-NO_2$ over the 1-year period exhibited a linear

558   relationship with a fair correlation ($R = 0.41$), and daily mean $PC-NO_2$ vs. $SI-NO_2$ exhibited a

559   good linear correlation ($R = 0.73$), supporting the overall uniformity of NO_2 profiles in the PBL

560   over Seosan despite the continuous impact of LPS emissions.

561   The impact of meteorological conditions on the relationship between $PC-NO_2$ and $SI-NO_2$

562   was investigated through agglomerative hierarchical clustering, which indicated three

563   meteorological conditions: LD, MD, and SD. Under LD conditions, southerly winds advect

564   warm air under the upper ridge, forming stable and short PBLs and weak surface winds. By

565   contrast, under SD conditions, cold northerly winds induce unstable and high PBLs with strong

566   surface winds. The correlations between daily mean $PC-NO_2$ and $SI-NO_2$ levels, and their

567   variation during 1100–1700 KST, weakened under LD conditions, suggesting that the shape of

568   the NO_2 profile typically deviates from a uniform profile under SD and MD conditions. Aircraft

569   measurements under LD conditions demonstrated NO_2 plumes aloft, with anomalous vertical

570   structures and different horizontal (latitudinal) gradients of surface NO_2 at higher altitudes,

571   such as 600 m over Seosan.

572   Thus, the relationship between $PC-NO_2$ and $SI-NO_2$ depends on the presence of NO_2

573   plumes aloft under LD conditions, which provide a favorable environment for LPS plumes

574   decoupled from the surface at Seosan. Our findings suggest that the correlation between PC-

575   NO_2 and $SI-NO_2$ may serve as an indicator of the degree of complexity of urban air quality.

576   This correlation can be optimally applied for air quality evaluation and vertical analysis by

577   combining the Pandora Asia Network with AQM networks, and the results can be also applied

578   to environmental GEMS observation analysis in combination with SI observations. More

579   detailed studies on urban air pollution evaluation will be undertaken based on PC, DOAS,

580 aircraft, SI air quality, and surface turbulence observation data, as well as modeling studies of

581 data collected during the GMAP-2021 campaign.

582

592

593 **Data Availability.**

594 The measurements can be accessed by contacting the corresponding authors.

595

596 **Competing interest.**

597 The authors declare that they have no conflict of interest.

598

599 **Author Contributions.**

600 Lim-Seok Chang: Conceptualization, Formal analysis, Visualization, Investigation, Writing -

601 Original draft; Donghee Kim, Hyunkee Hong, Deok-Rae Kim, Jeonga Yu, and Daewon Kim; Data

602 curation; Hanlim Lee, Kwangyul Lee, and Jinkyu Hong: Methodology and formal analysis; Hyun-

603 Young Jo: Formal analysis and Visualization; Cheol-Hee Kim ; Writing—original draft preparation,

604 Writing—review and editing. All authors have read and agreed to the published version of the

605   manuscript.

606   **References**

607   Biggs, W.G. and Graves, M.E.: A lake breeze index, J. Appl. Meteor., 1, 474–480,

608   http://www.jstor.org/stable/26169480, 1962.

609   Boersma, K.F., Jacob, D.J., Trainic, M., Rudich, Y., DeSmedt, I., Dirksen, R., and Eskes, H.J.:

610   Validation of urban NO_2 concentrations and their diurnal and seasonal variations observed from the

611   SCIAMACHY and OMI sensors using in situ surface measurements in Israeli cities. Atmos. Chem.

612   Phys., 9, 3867–3879, https://doi.org/10.5194/acp-9-3867-2009, 2009.

613   Cede A.: Manual for Blick Software Suite 1.7, Tech. rep., LuftBlick, Austria, 161 pp., 2019.

614   Chong, H., Lee, H., Koo, J.H., Kim, J., Jeong, U., Kim, W., Kim, S.W., Herman, J.R., Abuhassan, N.K.,

615   Ahn, J.Y., Park, J.H., Kim, S.K., Moon, K.J., Choi, W.J., and Park, S.S.: Regional characteristics

616   of NO_2 column densities from Pandora observations during the MAPS-Seoul campaign, Aerosol

617   Air Qual. Res. 18, 2207–2219, https://doi.org/10.4209/aaqr.2017.09.0341, 2018.

618   Engel-Cox, J.A., Holloman, C.H., Coutant, B.W., and Hoff, R.M.: Qualitative and quantitative

619   evaluation of MODIS satellite sensor data for regional and urban scale air quality, Atmos. Environ.,

620   38, 2495–2509, http://dx.doi.org/10.1016/j.atmosenv.2004.01.039, 2004.

621   Flynn, C.M., Pickering, K.E., Crawford, J.H., Weinheimer, A.J., Diskin, G., Thornhill, K.L., Loughner,

622   C., Lee, P., and Strode, S.A.: Variability of O_3 and NO_2 profile shapes during DISCover-AQ:

623   Implications for satellite observations and comparisons to model-simulated profiles, Atmos.

624   Environ., 147, 133–156, https://doi.org/10.1016/j.atmosenv.2016.09.068, 2016.

625   Herman, J., Cede, A., Spinei, E., Mount, G., Tzortziou, M., and Abuhassan, N.: NO_2 column amounts

626   from ground-based Pandora and MFDOAS spectrometers using the direct-sun DOAS technique:

627   Intercomparisons and application to OMI validation, J. Geophys. Res. Atmos, 114, D13307,

628   https://doi.org/10.1029/2009JD011848, 2009.

Herman, J., Spinei, E., Fried, A., Kim, J., Kim, J., Kim, W., Cede, A., Abuhassan, N., and Rozenhaimer, S.M.: NO$_2$ and HCHO measurements in Korea from 2012 to 2016 from Pandora spectrometer instruments compared with OMI retrievals and with aircraft measurements during the KORUS-AQ campaign, Atmos. Meas. Tech., 11, 4583–4603, https://doi.org/10.5194/amt-11-4583-2018, 2018.

Hong, J.-W., Lee, S.-D., Lee, K., and Hong, J.: Seasonal variations in the surface energy and CO$_2$ flux over a high-rise, high-population, residential urban area in the East Asian monsoon region, Int. J. Climatol., 40, 4384–4407, https://doi.org/10.1002/joc.6463, 2019.

Jo, H.-Y. and Kim, C.-H: Identification of long-range transported haze phenomena and their meteorological features over Northeast Asia, J. Appl. Meteorol. Climatol., 52(6), 1318–1328, https://doi.org/10.1175/JAMC-D-11-0235.1, 2013.

Kim, C.-H., Lee, H.-J., Kang, J.-E., Jo, H.-Y., Park, S.-Y., Jo, Y.-J., Lee, J.-J., Yang, G.-H., Park, T., and Lee, T.: Meteorological Overview and Signatures of Long-range Transport Processes during the MAPS-Seoul 2015 Campaign, Aerosol Air Qual. Res., 18, 2173–2184, https://doi.org/10.4209/aaqr.2017.10.0398, 2018.

Kim, C.-H., Park, S.-Y., Kim, Y.-J., Chang, L.-S., Song, S.-K., Moon, Y.-S., and Song, C.-K.: A Numerical Study on Indicators of Long-range Transport Potential for Anthropogenic Particle Matter over Northeast Asia, Atmos. Environ., 58, 35–44, https://doi.org/10.1016/j.atmosenv.2011.11.002, 2012.

Kim, J., Jeong, U., Ahn, M.-H., Park, R.J., Lee, H., Song, C.H., Choi, Y..-S., Lee. K.-H. Yoo, J.-M., Jeong. M.-J. Park, S.K., Lee, K.-M., Song, C.-K., Kim, S.-W., Kim, Y.J., Kim, S.-W., Kim, M., Go, S., Liu, X., Chance, K., Miller, C.C., Al-Saadi, J., Veihelmann, B., Bhartia, P.K., Torres, O., Abad, G.G., Haffner, D.P., Ko, D.H., Lee, S.H., Woo, J.-H., Chong, H., Park, S.S., Micks, D., Choi, W.J., Moon, K.-J., Veefkind, P., Levelt, P.F., Edwards, D.P., Kang, M., Eo, M., Bak, J., Baek, K., Kwon, H.-A., Yang, J., Park, J., Han, K.M., Kim, B.-R., Shin, H.-W., Choi, H., Lee, E., Chong, J., Cha, Y., Koo, J.-H., Hayashida, S., Kasai, Y., Kanaya, Y., Liu, C., Lin, J., Crawford, J.H., Carmichael, G.R.,

654   Newchurch, M.,J., Lefer, B.L., Herman, J.R., Swap, R.J., Lau, A.K.H., Kurosu, T.P., Jaross, G.,

655   Ahlers, B., Dobber, M., McElroy, T.C.., and Choi, Y.: New era of air quality monitoring from space:

656   Geostationary Environment Monitoring Spectrometer (GEMS), Bulletin of the American

657   Meteorological Society, 101(1), E1-E22, https://doi.org/10.1175/BAMS-D-18-0013.1, 2020.

658   Kim, S.-U., Kim, K.-Y.: Physical and chemical mechanisms of the daily-to-seasonal variation of PM_{10}

659   in Korea. Sci. Total Environ., 712, 136429, https://doi.org/10.1016/j.scitotenv.2019.136429, 2020.

660   Kim, S.-M., Koo, J.-H., Lee, H., Mok, J., Choi, M., Go, S., Lee, S., Cho, Y., Hong, J., and Seo, S.:

661   Comparison of $PM_{2.5}$ in Seoul, Korea Estimated from the Various Ground-Based and Satellite AOD,

662   Appl. Sci., 11(22), 10755, https://doi.org/10.3390/app112210755, 2021.

663   Lamsal, L.N., Martin, R.V., van Donkelaar, A., Celarier, E.A., Bucsela, E.J., Boersma, K.F., Dirksen,

664   R., Luo, C., and Wang, Y.: Indirect validation of tropospheric nitrogen dioxide retrieved from the

665   OMI satellite instrument: Insight into the seasonal variation of nitrogen oxides at northern

666   midlatitudes, J. Geophys. Res., 115, D05302, https://doi.org/10.1029/2009JD013351, 2010.

667   Lee, S., Kim, M., Kim, S.Y., Lee, D.W., Lee, H., Kim, J., Le, S., and Liu, Y.: Assessment of long-range

668   transboundary aerosols in Seoul, South Korea from Geostationary Ocean Color Imager (GOCI) and

669   ground-based observations, Environ. Pollut., 269, 115924,

670   https://doi.org/10.1016/j.envpol.2020.115924, 2021.

671   Lee, S.J., Lee, J., Greybush, S.J., Kang, M., and Kim, J.: Spatial and temporal variation in PBL height

672   over the Korean Peninsula in the KMA operational regional model, Adv. Meteorol., 2013(10), 1-

673   16, https://doi.org/10.1155/2013/381630, 2013.

674   National Institute of Environmental Research (NIER): Air Quality Monitoring Network Installation and

675   Operation. Ministry of the Environment, Seoul, Korea, 2021.

676   Sanchez, M.L., Pascual, D., Ramos, C. and Perez, I.: Forecasting particulate pollutant concentrations in

677   a city from meteorological variables and regional weather patterns, Atmos. Environ, 6, 1509–1519,

678   https://doi.org/10.1016/0960-1686(90)90060-Z, 1990.

679   Stohl, A., Eckhardt, S., Forster, C., James, P., and Spichtinger, N.: On the pathways and timescales of

680   intercontinental air pollution transport, J. Geophys. Res., 107(D23), 4684,

681   doi:10.1029/2001JD001396, 2002.

682   Sun, J., Lenschow, D.H., Mahrt, L., and Nappo, C.: The relationships among wind, horizontal pressure

683   gradient, and turbulent momentum transport during CASES-99, J. Atmos. Sci., 70, 3397–3414,

684   http://dx.doi.org/10.1175/JAS-D-12-0233.1, 2013.

685   Thompson, A.M., Stauffer, R.M., Boyle, T.P., Kollonige, D.E., Miyazaki, K., Tzortziou, M., Herman,

686   J.R., Abuhassan, N., Jordan, C.E., and Lamb, B.T.: Comparison of near-surface NO_2 pollution with

687   Pandora total column NO_2 during the Korea-United States Ocean Color (KORUS OC) Campaign,

688   J. Geophys. Res. Atmos.,124, 13560–13575, https://doi.org/10.1029/2019JD030765, 2019.

689   Van Roozendael, M. and Fayt, C.: WinDOAS Software user manual, Tech. rep., IASB/BIRA, Uccle,

690   Belgium, http://uv-vis.aeronomie.be/software/WinDOAS, 2001.

691   Venkat Reddy M., Vivekananda M. and Satish RUVN: Divisive Hierarchical Clustering with K-means

692   and Agglomerative Hierarchical Clustering, International Journal of Computer Science Trends and

693   technology, 5(5), 6–12, doi:10.17485/ijst/2016/v9is1/96012, 2017.

694   Wang, J., and Christopher, S.A.: Intercomparison between satellite-derived aerosol optical thickness

695   and $PM_{2.5}$ mass: Implications for air quality studies, Geophys. Res. Lett., 30, 2095,

696   https://doi.org/10.1029/2003GL018174, 2003.

697   Wang, Y., Dörner, S., Donner, S., Böhnke, S., Smedt, I.D., Dickerson, R.R., Dong, Z., He, H., Li, Z.,

698   Li, D., Ren, X., Theys, N., Wang, Y., Wang, Z., Xu, H., Xu, J., and Wagner, T.: Vertical profiles of

699   NO_2, SO_2, HONO, HCHO, CHOCHO and aerosols derived from MAX-DOAS measurements at a

700   rural site in the central western North China Plain and their relation to emission sources and effects

701   of regional transport, Atmos. Chem. Phys., 2, 5417–5449, http://dx.doi.org/10.5194/acp-19-5417-

702   2019, 2019.

703   Wenig, M., Spichtinger, N., Stohl, A., Held, G., Beirle, S., Wagner, T., Jahne, B., and Platt, U.:

704 Intercontinental transport of nitrogen oxide pollution plumes, Atmos. Chem. Phys., 3, 387–393,

705 SRef-ID: 1680-7324/acp/2003-3-387, 2003.

706 Zhao, X., Griffin, D., Fioletov, V., McLinden, C., Davies, J., Ogyu, A., Lee, S. C., Lupu, A., Moran,

707 M. D., Cede, A., Tiefengraber, M., and Müller, M.: Retrieval of total column and surface NO_2 from

708 Pandora zenith-sky measurements, Atmos. Chem. Phys., 19, 10619–10642,

709 https://doi.org/10.5194/acp-19-10619-2019, 2019.

710

711

712

713

714

715

716

717

718

719

720

721

722

723

724

725

726   **Table 1.** Summary of NO$_2$ column data from four Pandora (PA) measurement sites.

727   **Table 2.** Summary of aircraft measurements collected during the Geostationary Environment

728   Monitoring Spectrometer (GEMS) Map of Air Pollution (GMAP)-2020 campaign period

729   (November 12, 2020–January 20, 2021).

730

731

732

733

734

735

736   **Table 1.** Summary of NO$_2$ column data from four Pandora (PA) measurement sites.

Site	Site name	Site location		Mean (DU)	SD (DU)	Minimum (DU)	Maximum (DU)	Number of data points (days)	Operating period
		Longitude (°E)	Latitude (°N)						
PA$_1$	Seosan-DHJ	126.502	36.900	0.50	0.22	0.20	1.60	838 (11)	GMAP-2020 campaign
PA$_2$	Seosan-DM	126.458	36.778	0.43	0.19	0.18	1.62	1241 (13)	GMAP-2020 campaign
PA$_3$	Seosan-CC	126.449	36.785	0.40	0.14	0.18	0.97	1242 (13)	GMAP-2020 campaign
PA$_4$	Seosan-SS	127.492	36.777	0.39	0.16	0.17	1.79	8753 (141)*	1 year (Nov. 12, 2020–Oct. 30, 2021)

737   * The Pandonia Global Network (PGN) retrieval algorithm was applied to yearly
738   measurements.

739

740

741

742

31

743

Table 2. Summary of aircraft measurements collected during the Geostationary Environment Monitoring Spectrometer (GEMS) Map of Air Pollution (GMAP)-2020 campaign period (November 12, 2020–January 20, 2021).

Flight no.	Date	Meteorological classification
FL-1	Nov. 26, 2020	MD [1]
FL-2	Nov. 27, 2020	No Pandora measurements
FL-3	Nov. 28, 2020	MD
FL-4	Dec. 1, 2020	LD [2]
FL-5	Dec. 6, 2020	LD
FL-6	Dec. 8, 2020	LD
FL-7	Dec. 9, 2020	LD
FL-8	Dec. 12, 2020 (am)	MD
FL-9	Dec. 12, 2020 (pm)	MD

747   [1] LD: local wind-dominant conditions; [2] MD: mixed conditions.

748

749

750

751

Figure Captions

Figure 1. Map of sites used for Geostationary Environment Monitoring Spectrometer (GEMS) Map of Air Pollution (GMAP) campaigns conducted in (left) Seosan, South Korea in November 2020 to January 2021 (GMAP-2020), and (right) the Seoul metropolitan area from October 2021 to November 2021 (GMAP-2021). (Left) Measurement sites around Seosan, the study area for the GMAP-2020 campaign. Red circles indicate Pandora column measurement sites including (left) Seosan Daehoji (PA_1), Seosan Dongmun (PA_2), Seosan City Council (PA_3), and Seosan Super Site (PA_4). Blue triangles indicate large point sources (LPSs) including the Taean and Dangjin thermal power stations (LPS_1 and LPS_2, respectively), Hyundai steelworks (LPS_3), and Daesan petrochemical complex (LPS_4). Yellow squares indicate Automated Synoptic Observing System meteorological sites in Seosan (Met_1), AWS (Met_2), and buoy (Met_3). Green squares indicate air quality monitoring (AQM) network stations including Padori (AQM_1), Leewon (AQM_2), Taean (AQM_3), Daesan (AQM_4), Seongyeon (AQM_5), and Dongmoon (AQM_6). In the right panel, the black line indicates the route used for car-based differential optical absorption spectroscopy (Car-DOAS) measurements and the blue dotted line indicates the horizontal domain of Geo-CAPE airborne simulator (GCAS) measurements taken during the GMAP-2021 campaign.

Figure 2. Flight tracks for two Cessna Grand Caravan 208 B aircraft over Pandora sites (left) PA_4 and (right) PA_1 during the GMAP-2020 campaign. Colored circles indicate airborne NO_2 concentration observations. Stacked circles indicate spiral flights conducted over two sites.

Figure 3. (a) Pandora column (PC) NO_2 measurements as a function of surface *in situ* (SI) NO_2 observations at Pandora sites PA_1–PA_3 during the GMAP-2020 campaign and PA_4 during a 1-year period. A 1:1 linear regression model was used to evaluate the relationship between PC and SI measurements (black line). (b) Samplescatter plots of PC-NO_2 and SI-NO_2 for February 24 (red) and April 21 (blue), 2021.

Figure 4. K-means clustering yielded three groups of cases for (a) surface NO_2 and (b) PC-NO_2, associated with eight meteorological variables: (c) surface wind speed (Wsfc), (d) Psfc, (e) Psfc tendency (dPsfc/dt), (f) 925-hPa air temperature (T925), (g) 850-hPa wind speed (W850), (h) 850-hPa north–south wind component (NS850), (i) 850-hPa east–west wind component (EW850), and (j) 500-hPa geopotential height (GPH500). All data were de-

784 seasonalized using the 30-day moving average, except PC-NO_2, for which the monthly average

785 was used. (k) Simulated daily maximum mixing height (not directly clustered). (l) Box and

786 whisker plots of the sea breeze index (SBI) at Seosan for the 1-year period. Red dots indicate

787 the critical SBI (a value of 3), suggested by Biggs and Graves (1962).

788

789 **Figure 5.** (a) Scatterplots of daytime measurements at site PA$_4$ (a) PC-NO_2 vs. SI-NO_2 under

790 all meteorological conditions and (b) PC-NO_2 vs. Surface $\triangle NO_2$ in each meteorological

791 condition over a 1-year period (November 12, 2020–October 30, 2021). Here Surface $\triangle NO_2$

792 = SI-NO_2–(30-day moving average) SI-NO_2.

793

794 **Figure 6.** Box and whisker plots of diurnal variation in (a–c) PC-NO_2, (d–f) SI-NO_2, and (g–

795 i) surface O_3 under synoptic wind-dominant (SD), mixed (MD), and local wind-dominant (LD)

796 conditions in Seosan during a 1-year period (November 12, 2020–October 30, 2021).

797

798 **Figure 7.** Box and whisker plots of the vertical NO_2 and O_3 profiles measured by GMAP

799 aircraft superposed with *in situ* AQMS$_1$ measurements during flights (a, b) FL-5 (December 6)

800 and (d, e) FL-7 (December 6 and 9). Blue dashed lines are linear regression lines fitted to NO_2

801 and O_3 profiles within the planetary boundary layer (PBL). Black arrows indicate the simulated

802 PBL height (PBLH) obtained from the Korea Meteorological Administration (KMA).

803 HSYPLIT 24-h backward trajectories in Seosan are shown at altitudes of 100, 500, and 1,000

804 m, starting at 1600 KST on November 26 and 1200 KST on December 12.

805

806 **Figure 8.** Box and whisker plots of vertical profiles obtained from GMAP aircraft superposed

807 with *in situ* AQMS measurements for (1) NO_2 and (2) O_3 for flights (a) FL-1 (November 26),

808 (b) FL-3 (November 28), and (c) FL-8 (December 12). Blue dashed lines are linear regression

809 lines fitted to NO_2 and O_3 in the PBL. Black arrows indicate PBLH simulated by the Hybrid

810 Single-Particle Lagrangian Integrated Trajectory (HYSPLIT) Global Forecast System (GFS).

811

812 **Figure 9.** Time series and scatterplots of PC-NO_2 and SI-NO_2 at PA$_2$ on (a) December 6, (b)

813 December 9, (c) November 26, and (d) December 12. (e) Scatterplot of PC-NO_2 and SI-NO_2

814 on December 6 (blue), December 9 (red), November 26 (gray), and December 12 (black). (f)

815 Vertical potential temperature profiles on December 6, 9, and 12, 2020. Radiosonde data for
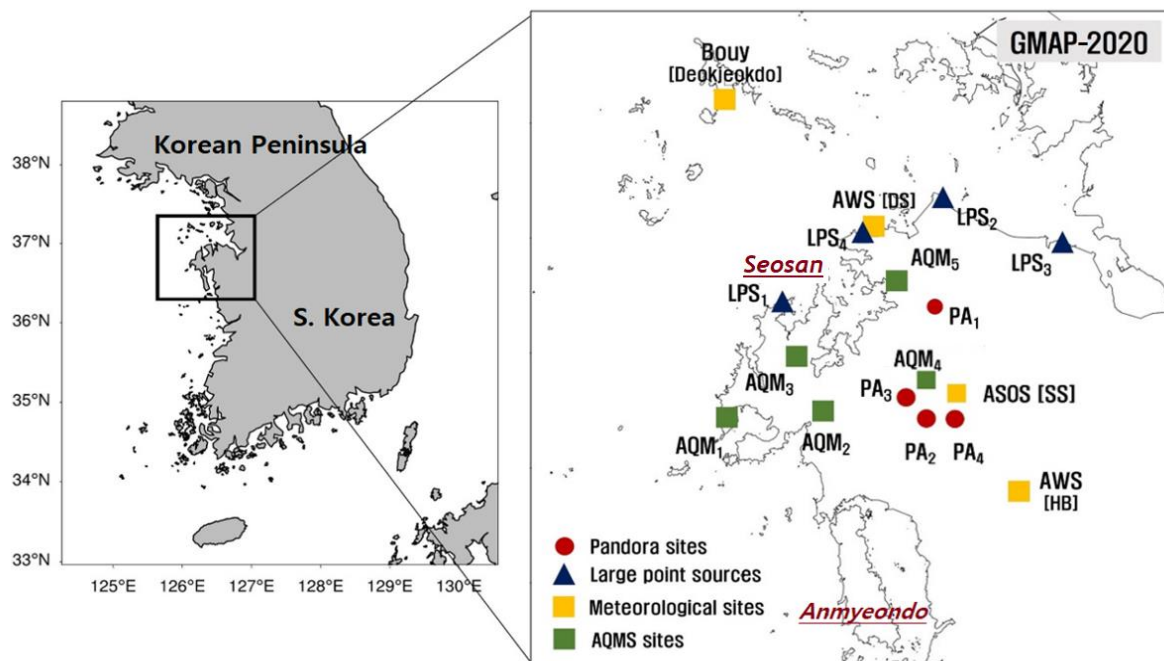
816 November 26, 2020 are missing.

817

818 **Figure 10.** Latitudinal NO_2 distribution at the surface and 600 m over PA_4 (Seosan Super Site),

819 averaged during (a) 1300–1600 KST on December 6 (FL-5) by longitude and (b) 1200–1400

820 KST on December 9 (FL-7) by latitude, obtained from airborne (blue) and surface

821 measurements (red).

822

823 **Figure 11.** Examples of the diurnal variation on November 25 (a, c, e) and December 14 (b, d,

824 f). (a, b) Column NO_2 at sites PA_1–PA_4 and surface NO_2 at air quality monitoring sites AQM_4

825 and AQM_6. (c, d) Sensible heat fluxes and surface wind speed at PA_4. (e, f) Diurnal variation

826 in NO_2, NO_2^-, and O_3 normalized by CO. Figure 1 shows the locations of the measurement

827 sites.

828

829

830

831

832

833

834

835

836

837

838

839

840

841

842

843

844

845

846

Figure 1. Map of sites used for Geostationary Environment Monitoring Spectrometer (GEMS) Map of Air Pollution (GMAP) campaigns conducted in (left) Seosan, South Korea in November 2020 to January 2021 (GMAP-2020), and (right) the Seoul metropolitan area from October 2021 to November 2021 (GMAP-2021). (Left) Measurement sites around Seosan, the study area for the GMAP-2020 campaign. Red circles indicate Pandora column measurement sites including (left) Seosan Daehoji (PA_1), Seosan Dongmun (PA_2), Seosan City Council (PA_3), and Seosan Super Site (PA_4). Blue triangles indicate large point sources (LPSs) including the Taean and Dangjin thermal power stations (LPS_1 and LPS_2, respectively), Hyundai steelworks (LPS_3), and Daesan petrochemical complex (LPS_4). Yellow squares indicate Automated Synoptic Observing System meteorological sites in Seosan (Met_1), AWS (Met_2), and buoy (Met_3). Green squares indicate air quality monitoring (AQM) network stations including Padori (AQM_1), Leewon (AQM_2), Taean (AQM_3), Daesan (AQM_4), Seongyeon (AQM_5), and Dongmoon (AQM_6). In the right panel, the black line indicates the route used for car-based differential optical absorption spectroscopy (Car-DOAS) measurements and the blue dotted line indicates the horizontal domain of Geo-CAPE airborne simulator (GCAS) measurements taken during the GMAP-2021 campaign.

862

863

864

865

Figure 2. Flight tracks for two Cessna Grand Caravan 208 B aircraft over Pandora sites (left) PA$_4$ and (right) PA$_1$ during the GMAP-2020 campaign. Colored circles indicate airborne NO$_2$ concentration observations. Stacked circles indicate spiral flights conducted over two sites.

872

Figure 3. a) Pandora column (PC) NO$_2$ measurements as a function of surface *in situ* (SI) NO$_2$ observations at Pandora sites PA$_1$–PA$_3$ during the GMAP-2020 campaign and PA$_4$ during a 1-year period. A 1:1 linear regression model was used to evaluate the relationship between PC and SI measurements (black line). (b) Sample scatterplots of PC-NO$_2$ and SI-NO$_2$ for February 24 (red) and April 21 (blue), 2021.

Figure 4. K-means clustering yielded three groups of cases for (a) surface NO_2 and (b) PC-NO_2, associated with eight meteorological variables: (c) surface wind speed (Wsfc), (d) Psfc, (e) Psfc tendency (dPsfc/dt), (f) 925-hPa air temperature (T925), (g) 850-hPa wind speed (W850), (h) 850-hPa north–south wind component (NS850), (i) 850-hPa east–west wind component (EW850), and (j) 500-hPa geopotential height (GPH500). All data were de-seasonalized using the 30-day moving average, except PC-NO_2, for which the monthly average was used. (k) Simulated daily maximum mixing height (not directly clustered). (l) Box and whisker plots of the sea breeze index (SBI) at Seosan for the 1-year period. Red dots indicate the critical SBI (a value of 3), suggested by Biggs and Graves (1962).

Figure 5. (a) Scatterplots of daytime measurements at site PA$_4$ (a) PC-NO$_2$ vs. SI-NO$_2$ under all meteorological conditions and (b) PC-NO$_2$ vs. Surface $\triangle$NO$_2$ in each meteorological condition over a 1-year period (November 12, 2020–October 30, 2021). Here Surface $\triangle$NO$_2$ = SI-NO$_2$ – (30-day moving average) SI-NO$_2$.

916

Figure 6. Box and whisker plots of diurnal variation in (a–c) PC-NO$_2$, (d–f) SI-NO$_2$, and (g–i) surface O$_3$ under synoptic wind-dominant (SD), mixed (MD), and local wind-dominant (LD) conditions in Seosan during a 1-year period (November 12, 2020–October 30, 2021).

917
918
919
920
921
922
923
924
925
926

929

Figure 7. Box and whisker plots of the vertical NO_2 and O_3 profiles measured by GMAP aircraft superposed with *in situ* $AQMS_1$ measurements during flights (a, b) FL-5 (December 6) and (d, e) FL-7 (December 6 and 9). Blue dashed lines are linear regression lines fitted to NO_2 and O_3 profiles within the planetary boundary layer (PBL). Black arrows indicate the simulated PBL height (PBLH) obtained from the Korea Meteorological Administration (KMA). HSYPLIT 24-h backward trajectories in Seosan are shown at altitudes of 100, 500, and 1,000 m, starting at 1600 KST on November 26 and 1200 KST on December 12.

937

938

939

940
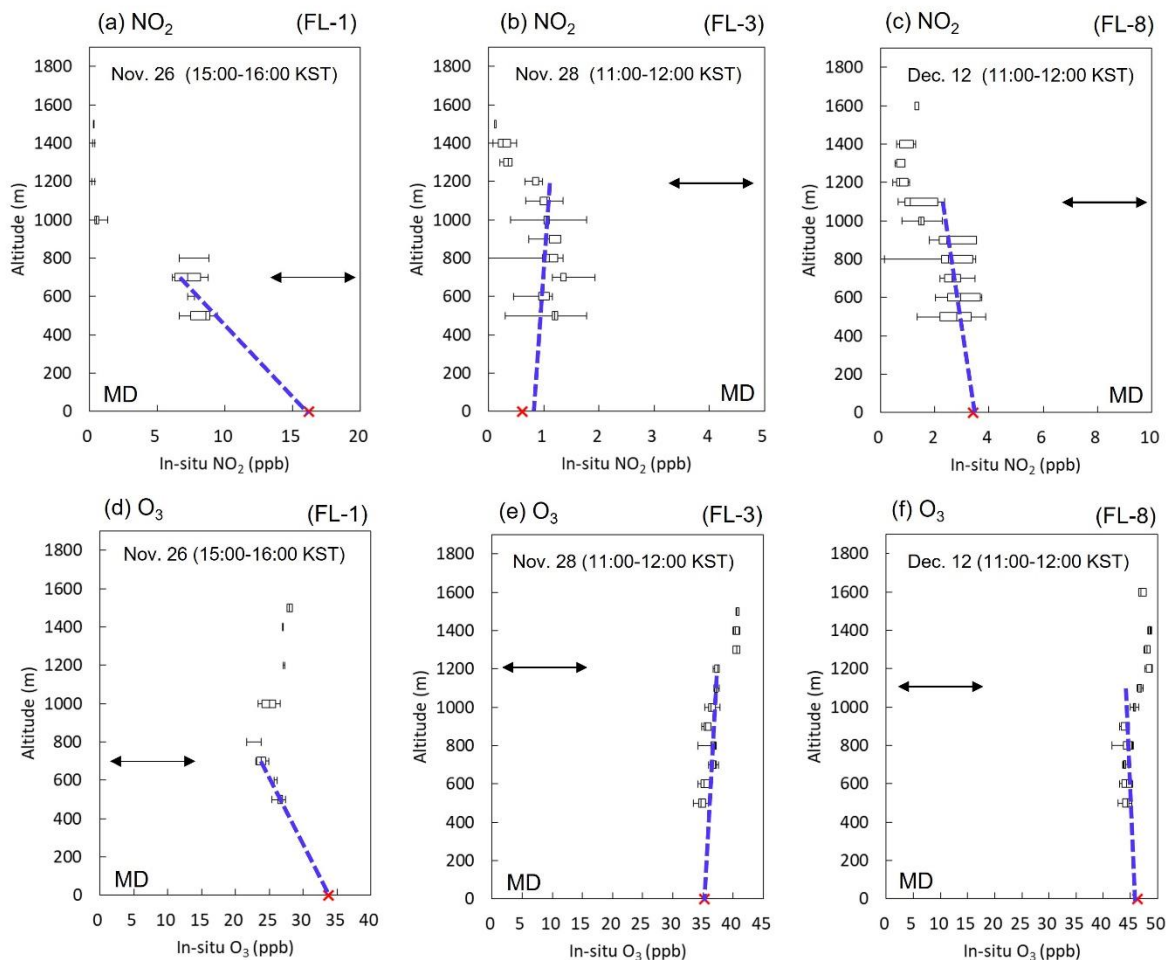
941

942

Figure 8. Box and whisker plots of vertical profiles obtained from GMAP aircraft superposed with *in situ* AQMS measurements for (1) NO_2 and (2) O_3 for flights (a) FL-1 (November 26), (b) FL-3 (November 28), and (c) FL-8 (December 12). Blue dashed lines are linear regression lines fitted to NO_2 and O_3 in the PBL. Black arrows indicate PBLH simulated by the Hybrid Single-Particle Lagrangian Integrated Trajectory (HYSPLIT) Global Forecast System (GFS).
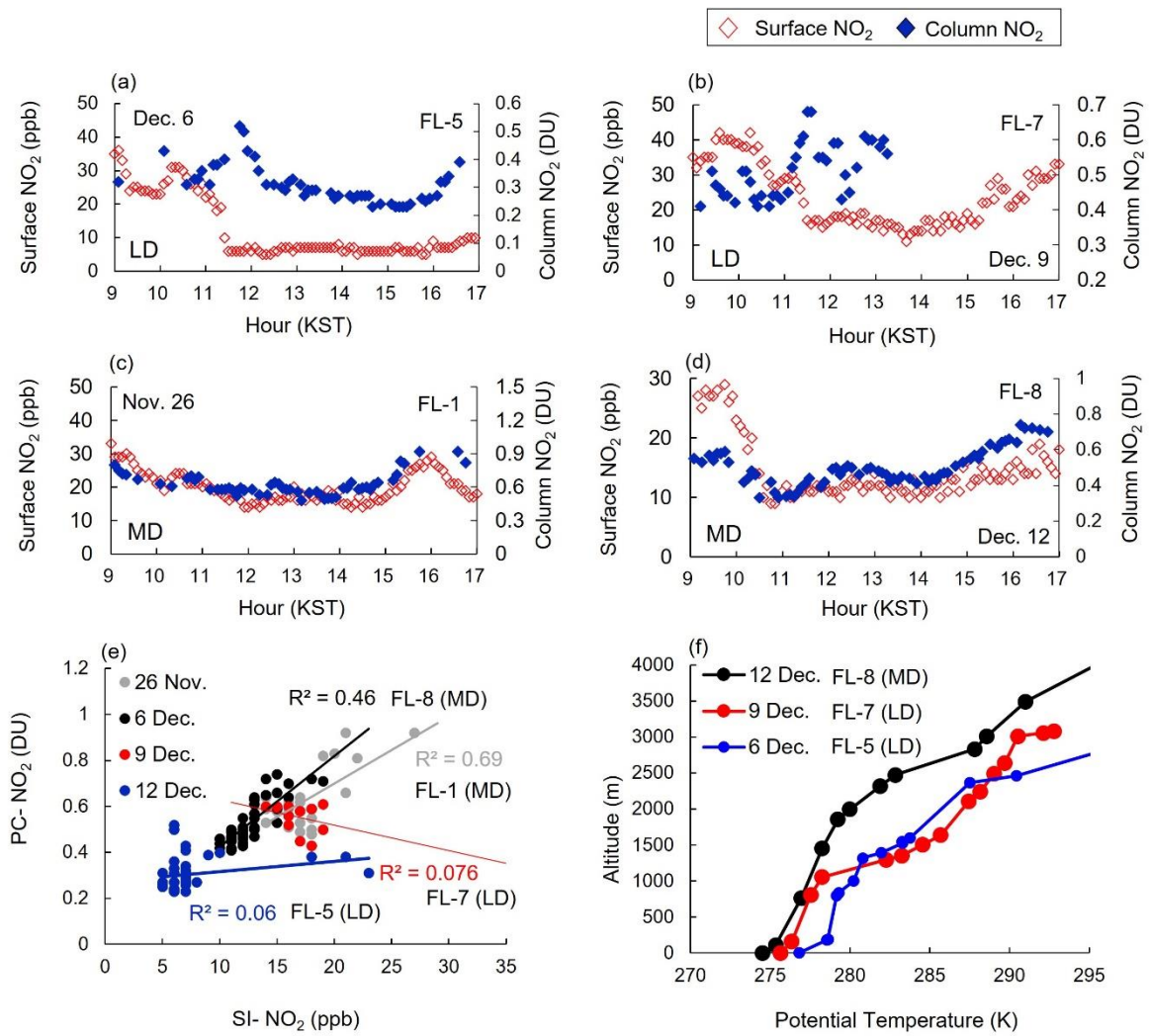
948

949

950

951

952

953

Figure 9. Time series and scatterplots of PC-NO$_2$ and SI-NO$_2$ at PA$_2$ on (a) December 6, (b) December 9, (c) November 26, and (d) December 12. (e) Scatterplot of PC-NO$_2$ and SI-NO$_2$ on December 6 (blue), December 9 (red), November 26 (gray), and December 12 (black). (f) Vertical potential temperature profiles on December 6, 9, and 12, 2020. Radiosonde data for November 26, 2020 are missing.
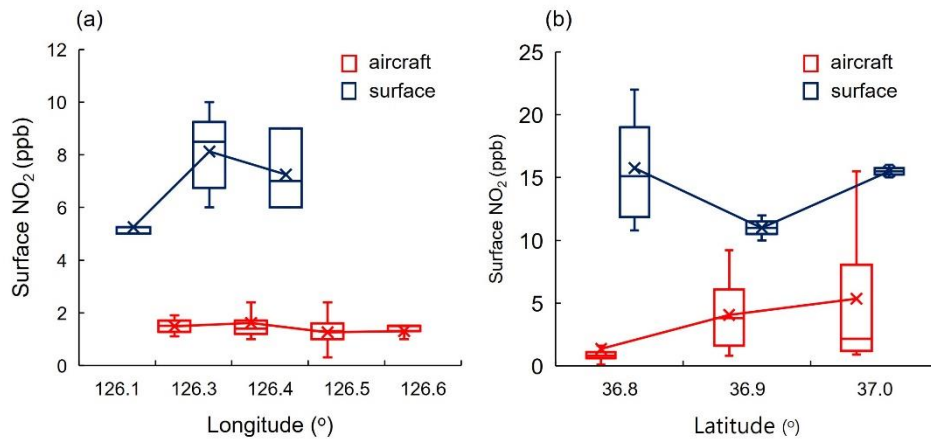
Figure 10. Latitudinal NO_2 distribution at the surface and 600 m over PA4 (Seosan Super Site), averaged during (a) 1300–1600 KST on December 6 (FL-5) by longitude and (b) 1200–1400 KST on December 9 (FL-7) by latitude, obtained from airborne (blue) and surface measurements (red).
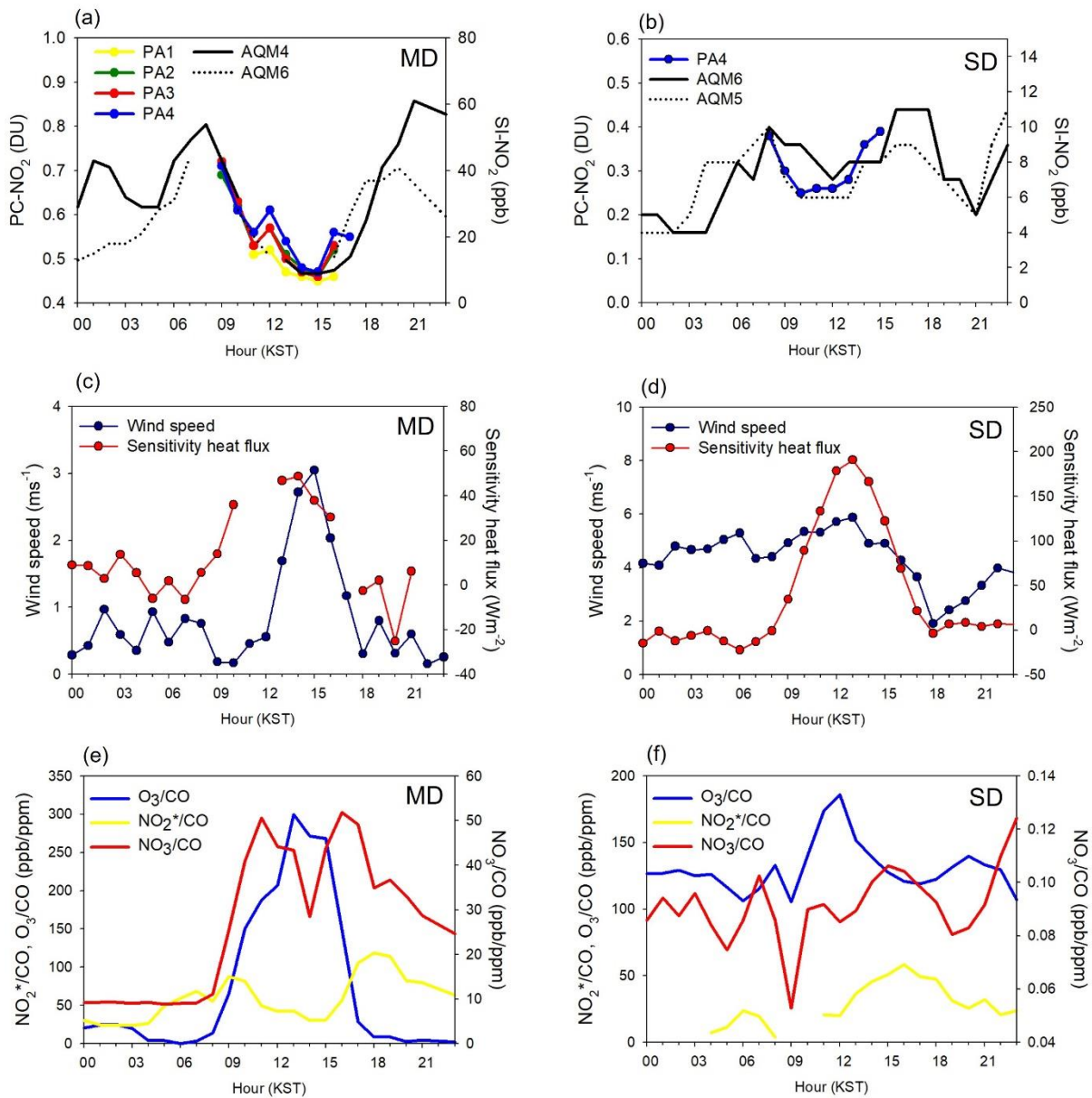
Figure 11. Examples of the diurnal variation on November 25 (a, c, e) and December 14 (b, d, f). (a, b) Column NO_2 at sites PA_1–PA_4 and surface NO_2 at air quality monitoring sites AQM_4 and AQM_6. (c, d) Sensible heat fluxes and surface wind speed at PA_4. (e, f) Diurnal variation in NO_2, NO_2^-, and O_3 normalized by CO. Figure 1 shows the locations of the measurement sites.